ARTICLE

Check for updates

Hydrodynamic pursuit by cognitive self-steering microswimmers

Segun Goh [1], Roland G. Winkler [1] & Gerhard Gompper [1✉]

The properties of biological microswimmers are mostly determined by fluid-mediated interactions, which govern their propulsion, perception of their surrounding, and the steering of their motion for pursuit. Transferring similar functionalities to synthetic microswimmers poses major challenges, and the design of favorable steering and pursuit strategies is fundamental in such an endeavor. Here, we employ a squirmer model to investigate the pursuit of pursuer-target pairs with an implicit sensing mechanism and limited hydrodynamic steering abilities of the pursuer. Two hydrodynamic steering strategies are studied for the pursuer's propulsion direction by adaptation of its surface flow field: reorientation toward the target with limited maneuverability, and alignment with the target's propulsion direction combined with speed adaptation. Depending on the nature of the microswimmer propulsion (puller, pusher) and the velocity-adaptation scheme, stable cooperatively moving states can be achieved, where pursuer and target mutually affect their motion and trajectories.

[1] Theoretical Physics of Living Matter, Institute of Biological Information Processing and Institute for Advanced Simulation, Forschungszentrum Jülich, 52425 Jülich, Germany. ✉email: g.gompper@fz-juelich.de

The vast majority of motile biological microorganisms, such as bacteria, algae, or heterotrophic nanoflagellates, exploit fluid-mediated interactions for their propulsion, sensing of obstacles and prey, and feeding[1–3]. Their micrometer size, which implies low-Reynolds-number fluid dynamics, where viscosity dominates over inertia, and strong thermal fluctuations[4,5], render an efficient hunting particularly difficult. An example is hydrodynamic starvation of larval fishes, where hydrodynamic flow fields limit their feeding performance[6]. Another example is ambush-feeding, e.g., of copepods, which sense the hydrodynamic disturbances generated by the swimming prey and attack quickly[7]. Here, it is unclear how such microswimmers avoid warning the prey by hydrodynamic disturbances and pushing it away while attacking. Evidently, microscale predators are able to adjust their locomotion upon the sensed and gathered information to favorably approach the prey. Moreover, hydrodynamic interactions play a major role in the collective behavior of microswimmers[8–10]. This is paradigmatically reflected in the behavior of bacteria with their large-scale swarming motion and active turbulence[9,11–13]. However, the role of signal exchange, aside from hydrodynamics, between microswimmers and of the corresponding adaption of motion, and its effect on the emergent cooperative and collective behaviors is an issue which goes far beyond, and remains to be elucidated and understood.

Similar questions arise in the design of synthetic intelligent micromachines (microbots), either via biomimetics of biological microswimmers, e.g., flagellated swimmers[14,15], or by suitable colloidal realizations[16–19]. Here, sensing and adaptation of motion is often achieved by stimuli via external fields[16,17]. Yet, paramount to perform complex tasks in biomedical and environmental applications is their ability to suitably adopt their motion to the changing surroundings along their trajectories[20,21]. This can be achieved by equipping the microbots either with engineered or biological actuators and sensors[15,22].

How can directional sensing be achieved in agents as small as microorganisms and microbots? Visual perception requires a minimum swimmer size, which can be as small as a few millimeters, as in zebra fish larvae[23] and some copepods[24]. These larvae are too large and swim too fast to be in the low-Reynolds-number regime; estimates are in the range of $60 < \text{Re} < 1400$, which indicates that inertia plays a significant role in the dynamics[25]. On smaller scales, the perception of chemical gradients can be employed, which is used by sperm to find the egg[26], and by neutrophils to chase bacteria in blood[27]. Engineered microbots can employ external vision, cognition, and steering to perform tasks like pushing a load[28] and performing collective motion in fluid environments[18].

In the strive for the design of intelligent — sensing, cognitive, self-steering, and adaptive — microswimmers[29–31], knowledge of favorable propulsion and steering mechanism is fundamental. A priori insight into emergent behaviors for a particular adaptation scheme would be beneficial for a desired performance, in particular, when hydrodynamic interactions and thermal noise play a major role.

Here, we explore strategies and present simulation results for the pursuit by two types of microswimmers immersed in a fluid. We employ a generic model of microswimmers, squirmers[32–34], where the pursuer is equipped with implicit sensing and hydrodynamic response and adaptation mechanisms. Two different steering schemes are considered, extensions of the minimal cognitive flocking model—active Brownian particles (ABPs), augmented by active reorientation of their directions of motion toward a moving object[35–38]—, and of a hydrodynamic Vicsek model[39–42]—microswimmers which tend to align their swimming direction with their neighbors, augmented with speed adaptation. We denote these self-steering microswimmers *intelligent* squirmers (iSquirmers). For comparison, we also perform simulations of self-steering, intelligent active Brownian particle (iABP) pairs, in particular, to resolve the effect of steric interactions on the microswimmer motion. Our simulations yield stable and unstable cooperative states, which strongly depend on the type of swimmer flow field (puller, pusher), and favorable choices of squirmer flow-field properties and steering suggest strategies for their stable motion and possibilities for target steering.

In our modeling approach, we use a simple (non-linear) response function, which relates the adaption of motion to the input signal. We would like to emphasize that the concept of cognition has been extended recently to aneural systems, including bacteria, plants, even to all living organisms[43,44], and similarly to autonomous machines and (micro)robots[45,46]. Our minimal modeling approach differs in cognitive capacity and complexity—but not in its conceptual strategy—from much more powerful cognitive units, such as macroscopic robots and many animals. An alternative approach to derive more complex cognitive relations is machine learning[47,48]. Other, more complex sensing and searching strategies have also been studied, at the level of individuals in complex environments[49,50], as well as in systems of groups of information-processing agents without hydrodynamic interactions[51,52].

Results

Model of self-steering microswimmer. A microswimmer is modeled as a spherical and neutrally buoyant squirmer[8,32,33,53,54]. The propulsion and steering are realized by an imposed surface flow field (slip velocity)[34]. Two types of particles are considered: pursuer (iSquirmer) and target, see Fig. 1a for illustration of the geometry. The target is propelled by a prescribed flow field along a body-fixed direction $\mathbf{e}_t$ with the swim speed v_t, and moves, in absence of noise, along a trajectory with simple geometry (straight or helical). Moreover, the surface flow field, described by the first two Legendre polynomials, creates an active stress, whose strength is characterized by the parameter β, where $\beta < 0$ corresponds to a pusher and $\beta > 0$ to a puller (cf. Methods Section). In contrast, the pursuer, with a body-fixed direction vector $\mathbf{e}_p$ and swim speed v_p, is propelled by a non-axisymmetric flow field (Fig. 1b, c). As a consequence, the pursuer moves on a helical trajectory in general. Pursuit of the target is achieved by adaptation of the pursuer's rotational motion via the non-axisymmetric flow modes, such that $\mathbf{e}_p$ is redirected toward the desired direction. The required angular velocity $\boldsymbol{\omega}_0$ to turn the pursuer's propulsion direction $\mathbf{e}_p$ toward a desired direction $\mathbf{e}_{\text{aim}}$ can be written as

$$\boldsymbol{\omega}_0 = C_0 \mathbf{e}_p \times \mathbf{e}_{\text{aim}}, \qquad (1)$$

where C_0 controls the strength of actuation via non-axisymmetric components of surface flow field (cf. Methods Section, Eqs. (10)–(12)). Self-propulsion and self-steering of pursuers are characterized by the Péclet number Pe and the maneuverability Ω via

$$\text{Pe} = \frac{v_p}{\sigma D_R} \quad \text{and} \quad \Omega = \frac{C_0}{D_R}, \qquad (2)$$

where σ denotes the diameter of a squirmer, and $D_R = k_B T / (\pi \eta \sigma^3)$ the rotational diffusion coefficient with fluid viscosity η. The embedding fluid is described by a particle-based mesoscale hydrodynamics simulation technique – the multiparticle collision dynamics approach –, which captures the properties of fluctuating hydrodynamics[55–59]. Pursuer and target also experience hard-core repulsion to describe volume exclusion.

The goal of our study is, on the one hand, to provide insight into the emergent dynamics of the squirmer pursuer-target pair,
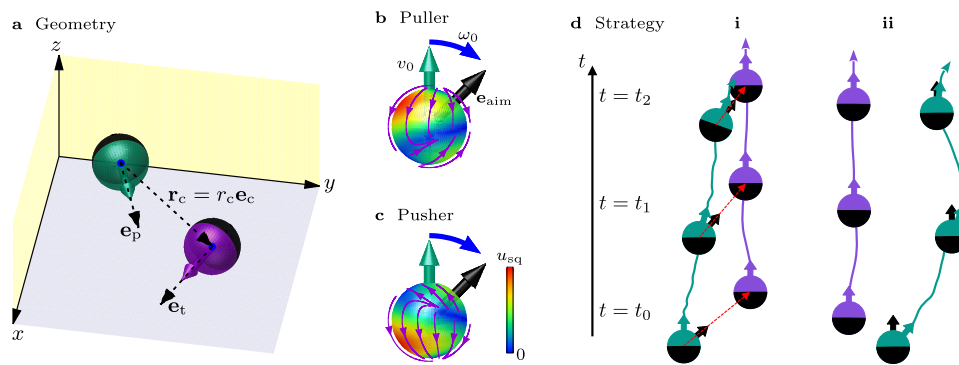
Fig. 1 Illustration of the squirmers. a The spherical pursuer (petrol) and target (purple) squirmers with the center-to-center difference vector $\mathbf{r}_c$ are self-propelled in the directions $\mathbf{e}_p$ and $\mathbf{e}_t$, respectively. **b, c** Puller and pusher surface flow fields steering the propulsion direction $\mathbf{e}_p$ in the direction $\mathbf{e}_{aim}$ via rotation around the vector $\boldsymbol{\omega}_0$ of frequency ω_0. **d** Schematic illustration of the steering strategies. Black bold arrows represent $\mathbf{e}_{aim}$ for each strategy; red dashed arrows indicate $\mathbf{r}_c = r_c \mathbf{e}_c$ where $r_c \equiv |\mathbf{r}_c|$. **d-i** For the strategy of reorientation toward the target position, i.e., $\mathbf{e}_{aim} = \mathbf{e}_c$, the pursuer automatically approaches the target, forming a head-to-tail configuration. **d-ii** Alignment strategy with $\mathbf{e}_{aim} = \mathbf{e}_t$.

and, on the other hand, to evaluate preferential pursuit strategies. We focus on three scenarios: (i) The pursuit of a target moving on a noisy, approximately straight trajectory. Here, the pursuer aims for the target and the speed ratio $\alpha = v_t/v_p$ is varied. (ii) The pursuit of a target moving on a noisy helical trajectory, where the helix slope $\xi = H/(2\pi R)$ is varied, where H is the helix pitch and R the helix radius. (iii) The pursuer aims to align its propulsion direction $\mathbf{e}_p$ parallel to $\mathbf{e}_t$ and adjusts its propulsion velocity to stay close to the target. The aiming strategy applied for scenarios (i) and (ii), and the alignment strategy for scenario (iii) are illustrated in Fig. 1d-i, d-ii, respectively. We investigate not only the transient dynamics of capturing the target, but, more importantly, also the stable cooperative motion, which is essential for designing microrobots that are capable of performing long-term stable tasks, e.g., cargo transportation. The emergent dynamics of the pair is strongly affected by the interfering flow fields. In particular, the variation of the squirmer velocities is tightly connected with a change of their force-dipole strength, because β is fixed, and a vanishing swimming velocity implies a vanishing active stress[60].

Noisy, approximately straight target trajectory. The cooperative motion of pairs of non-steering squirmers has been analyzed in detail, both theoretically[53,61] and by simulations[61–64]. In absence of thermal fluctuations, short-time stable attractive hydrodynamic interactions are predicted for parallel propulsion directions, when pullers move in a head-to-tail and pushers in a side-by-side configuration. However, the long-time asymptotic interaction between two squirmers is always repulsive, even though the transient regime can be rather long[61]. Thermal fluctuations destabilize even the short-time cooperative motion, and the trajectories of two nearby squirmers diverge rather quickly[62–64]. Similarly, suspensions of aligned self-propelled particles are always unstable to fluctuations[40], and a hydrodynamic instability due to particle active stresses is predicted for pushers but not for pullers[65]. Hence, pursuit in absence of self-steering is essentially impossible, which would imply the extinction of any such dumb predator.

Self-steering of the pursuer toward the target changes the pursuit dynamics fundamentally, where the speed ratio α and the active stress play a decisive role for emerging stable cooperative states and a possible prey capture. For pullers ($\beta > 0$), pursuer-steering toward the target implies a preferential head-to-tail cooperative state. This favors stable touching pursuer-target configurations due to their attractive hydrodynamic flow fields (Fig. 2a-i). Our simulations yield stable pairs even for speed ratios

$1 < \alpha \lesssim 1.4$ for $\beta = 3$, i.e., for pursuer speeds smaller than the target speed (Fig. S1b, Supplementary Movie 1). Here, self-steering dominates over both, (thermal) fluid fluctuations as well as destabilizing hydrodynamic torques[53,61]. For $\alpha \gtrsim 1.4$, no long-time stable configurations are found. This finding is qualitatively consistent with far-field hydrodynamic predictions with the assumption of a parallel alignment of $\mathbf{e}_p$ and $\mathbf{e}_t$ (see Supplementary Note 1, Sec. S-IIA3), which suggest stable stationary-state configurations for

$$\alpha < \frac{(8/3)(r_c/\sigma)^2 + \beta}{(8/3)(r_c/\sigma)^2 - \beta}, \tag{3}$$

where σ and r_c denote the squirmer diameter and the instantaneous pursuer-target center-center distance, respectively (Fig. 1a). For $\beta = 3$ and a reasonably close distance $r_c/\sigma = 2$, Eq. (3) yields $\alpha < 1.78$, in semi-quantitative agreement with the simulation result (Fig. 2b). Such a distance dependence due to hydrodynamic effects implies a maximum initial separation between a pursuer-target pair, i.e., a capture distance, that allows the pursuer to reduce the initial gap and eventually to form a stable touching configuration (see Supplementary Note 1, Sec. S-IIC and Fig. S3, for details). In addition, Eq. (3) neglects noise, which reduces the hydrodynamic interactions by disturbing the head-to-tail configuration.

More challenging is the pursuit in case of pusher pairs ($\beta < 0$), because a head-to-tail configuration for the maneuverability $\Omega = 0$ is hydrodynamically unstable and squirmers repel each other. Yet, according to Eq. (3), stable pursuit is possible as long as $\alpha \lesssim 0.56$ for $\beta = -3$ and $r_c/\sigma = 2$, which roughly corresponds to the average distances between two pusher squirmers obtained in the simulations (see Fig. 2b). Indeed, our simulations confirm successful pursuit even for $\alpha \lesssim 0.8$ (see Fig. 2a-ii and Supplementary Movie 2). In the stationary state, the pursuer and target assume a finite average distance, as displayed in Fig. 2b, and the pursuer is not able to catch up with the target, but steering implies a stable cooperative state in a leader-follower arrangement. However, the pursuer hydrodynamically pushes the target, similarly to starving fish larvae, because its velocity is larger than that of the target. The average distance increases with increasing α, i.e., when the target speed is enhanced. Note that $\alpha = 0$ essentially corresponds to a resting target with the pursuer (noisily) circling around it and touching it for large velocities $v_p \rightarrow \infty$, or Péclet numbers (Eq. (2)). In the noise-free far-field limit, Eq. (3) yields the stationary-state pursuer-target distance
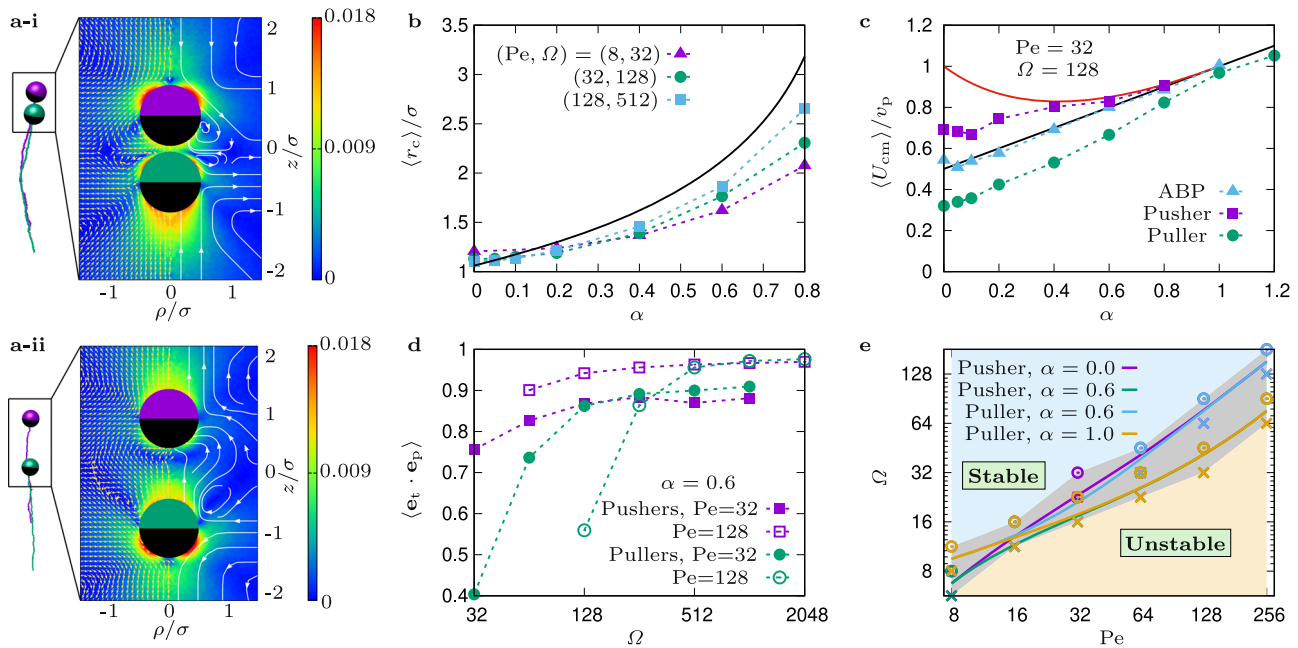
Fig. 2 Target on a noisy, approximately straight trajectory. a Illustration of pursuer-target-pair trajectories and flow fields for **a-i** pullers and **a-ii** pushers. **b** Average pursuer-target distance $\langle r_c \rangle$ for pushers as a function of the speed ratio $\alpha = v_t/v_p$ for the indicated combinations of Péclet number and maneuverability (symbols). The black solid line represents the far-field approximation $r_c = r_0$ of Eq. (4). **c** Center-of-mass speed of pursuer-target pairs for pushes (squares) and pullers (bullets). For comparison results of ABP pairs are shown (triangles). The black solid line indicates the speed $U_{cm} = v_p(1 + \alpha)/2$ and the red solid line the far-field approximation of Eq. (5). **d** Alignment parameter $\langle \mathbf{e}_p \cdot \mathbf{e}_t \rangle$ as a function of the maneuverability Ω for pushers (squares) and pullers (bullets) and the indicated Péclet numbers. No stable pairs are observed for Ω values smaller than $\Omega = 32$ for Pe $= 32$, $\Omega = 64$ (pushers) and $\Omega = 128$ (pullers) for Pe $= 128$. **e** State diagram, which displays the boundary between regions of stable and unsuccessful pursuit as a function of Pe and Ω, for pushers and pullers with various speed ratios α, as indicated. Pursuit is classified as unstable/unsuccessful when $r_c > 4\sigma$. Note that some symbols and lines lie on top of each other, in particular the data representing pusher pairs with $\alpha = 0.6$ and puller pairs with $\alpha = 1.0$ for Pe ≥ 32.

(see Supplementary Note 1, Eq. (S27))

$$r_c < r_0 = \sigma\sqrt{\frac{3\beta(\alpha + 1)}{8(\alpha - 1)}}, \qquad (4)$$

which qualitatively confirms our numerical result ($\beta = -3$), as displayed in Fig. 2b, where a pursuer has to be faster than the target, i.e., $\alpha < 1$, for stable pursuit.

The effect of this interference of the squirmers' hydrodynamic flow fields on the center-of-mass speed U_{cm} of the squirmer pair is displayed in Fig. 2c. In absence of active stress, the center-of-mass speed of the two squirmers would be $U_{cm} = (v_p + v_t)/2 = v_p(1 + \alpha)/2$, which increases linearly with α, in agreement with touching ABPs. Interference of the hydrodynamic flow fields leads to an enhancement of U_{cm} for pushers and reduction for pullers. The speed difference between pullers and pushers decreases with increasing α, and for $\alpha \gtrsim 0.8$ all swimmer types move with the same center-of-mass velocity. We like to emphasize that pushers are well separated for $\alpha \gtrsim 0.3$ (see Fig. 2b and S1**c-i**), and thus the target speed is enhanced via the fluid. It is this enhancement, which implies U_{cm} to be larger than for ABP pairs. With the assumption of pursuer-target arrangements with $\mathbf{e}_t \parallel \mathbf{e}_p \parallel \mathbf{r}_c$, the hydrodynamic far-field approximation yields the center-of-mass speed (see Supplementary Note 1, Eq. (S29))

$$\bar{v} = \frac{1 + \alpha^2}{1 + \alpha} v_p, \qquad (5)$$

which describes the simulation results very well for $\alpha > 0.6$ (see Fig. 2c). For $\alpha < 0.6$, $\mathbf{e}_t$ is neither well aligned with $\mathbf{e}_p$ nor with $\mathbf{r}_c$ (Fig. 2d and Fig. S1**a**), which violates the premises of the theoretical result and explains the deviations from $\bar{v}$. The dynamics of puller pairs is dominated by near-field

hydrodynamic effects, with attractive flow fields, which leads to U_{cm} to be smaller than for ABP pairs.

A crucial parameter in self-steering pursuit is the maneuverability Ω. By studying the dependence of the average distance $\langle r_c \rangle$ and the alignment parameter $\langle \mathbf{e}_p \cdot \mathbf{e}_t \rangle$ on the Péclet number and Ω, we can construct a phase diagram, which indicates the regions of stable and of unsuccessful pursuit. The dependence of the alignment of the propulsion directions $\mathbf{e}_t$ and $\mathbf{e}_p$ on the maneuverability is illustrated in Fig. 2d for the speed ratio $\alpha = 0.6$ and various Péclet numbers. For sufficiently large Ω, both pullers and pushers exhibit the same alignment parameter $\langle \mathbf{e}_p \cdot \mathbf{e}_t \rangle$, nearly independent of Pe, only slightly larger for larger Pe. Noteworthy is the decrease of alignment with decreasing Ω for pullers, where the drop appears at large Ω for larger Pe. Hence, Ω has to exceed a threshold value for a sufficiently strong alignment of the propulsion directions and the formation of stationary pairs. This is reflected in the phase diagram of Fig. 2e. Only for large maneuverability $\Omega \gtrsim$ Pe, the destabilizing effects of thermal fluctuations and hydrodynamic torques can be overcome and stable head-to-tail configuration can be achieved especially for pullers. Furthermore, the phase diagram shows that (i) pursuit is more difficult for smaller α (slower target), because the pursuer overshoots and circumvents slow targets with a long detour; (ii) pushers display a better pursuit performance than pullers for the same $\alpha = 0.6$, because near-field hydrodynamic effects hinder pullers with small maneuverability from forming head-to-tail configurations (see Supplementary Note 3, Fig. S6**b-v**).

Noisy helical target trajectory. By the nature of their flagella arrangement and the resulting chirality, bacteria often swim along helical trajectories rather than straight ones. For example, the flagella of E. coli bacteria form bundles, which can be inclined
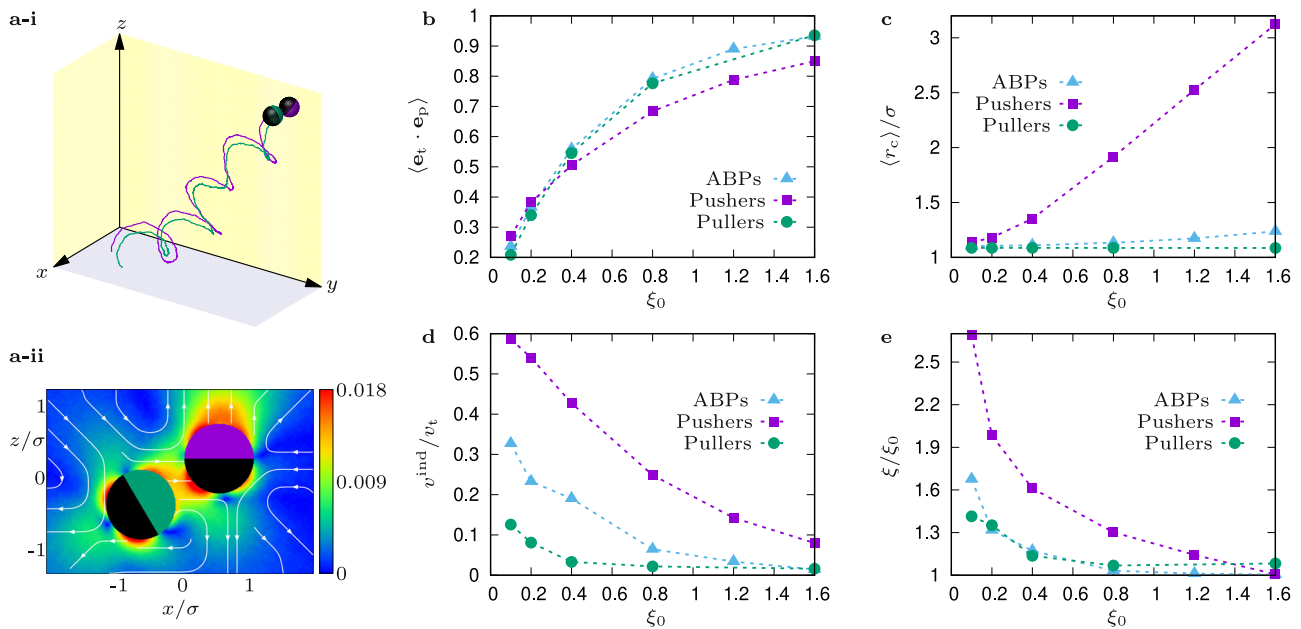
Fig. 3 Pursuer and target on helical target trajectory. a Illustration of pursuer-target-pair **a-i** trajectories and **a-ii** their flow field. **b** Order parameter $\langle \mathbf{e}_p \cdot \mathbf{e}_t \rangle$. **c** Mean pursuer-target distance, **d** hydrodynamic flow-field induced target velocity v^{ind}, and **e** effective helix slope ξ, as a function of the set slope $\xi_0 = H_0/(2\pi R_0)$ for pusher (purple squares), puller (green bullets), and ABP (blue triangles) pairs. The parameters are $\mathrm{Pe} = 128$, $\Omega = 8\,\Omega^{\mathrm{hel}}$, where $\Omega^{\mathrm{hel}} = \mathrm{Pe}/\sqrt{1+\xi_0^2}$ is the target angular velocity in units of D_R (Eqs. (9), (15), and (16)), $R_0 = \sigma$, and $\alpha = 1$.

with the cell body and, hence, lead to a wobbling motion along a helical trajectory[66–70]. There are many more chiral microswimmers in nature with correspondingly helical trajectories[10,71]. In such a situation, the pursuer and target do not have to move in a head-to-tail configuration, but the pursuer may follow a more favorable trajectory.

Figure 3a shows an example of the trajectories of a pursuer and a target and their flow field, where the latter moves on a helical trajectory of radius R and pitch H. Evidently, the pursuer traces the target on a helix with a radius, which is smaller than that of the target. Consequently, it traverses a shorter trajectory than the target, which allows the pursuer to follow the target even for speed ratios $\alpha > 1$. The particular arrangement is reflected in the relative orientation of the pursuer and target propulsion direction in Fig. 3b. For small helix slopes $\xi_0 = H_0/(2\pi R_0)$, where R_0 and H_0 are the radius and pitch of an individual noise-free target, respectively, $\mathbf{e}_p$ and $\mathbf{e}_t$ are almost orthogonal independent of the Péclet number (cf. Fig. S5**b**), but the propulsion directions become increasingly parallel with increasing ξ_0, which corresponds to a head-to-tail configuration. This applies to all swimmer types, pushers, pullers, and ABPs. In the limit $\xi_0 \to 0$ and small radii $R_0 \gtrsim \sigma$, the target moves along a circle with the pursuer located in its center and the propulsion direction is essentially pointing in the radial direction. The puller and ABP pursuer-target pairs touch each other (Fig. 3c, see also Supplementary Movie 3 for pullers), and steric interactions are important, which also affect the flow field of puller pairs, with an emerging Stokeslet flow field[64]. Even for pushers, this arrangement is particularly stable, because it reduces the pusher-pusher hydrodynamic repulsion. For large radii, $R_0 \gg \sigma$, the pursuer follows the target on a circle in a more head-to-tail configuration, as discussed above. With increasing ξ_0, the target trajectory straightens out. Pullers still attract each other and remain in a closely touching configuration for all ξ_0 (Fig. 3c). The average ABP pursuer distance increases slightly due to thermal fluctuations. Pronounced flow-field effects emerge for pushers, with a pursuer-target distance larger than their diameter. The increasing repulsive interactions for the

appearing head-to-tail configurations imply a substantial, almost linear growth of r_c for $\xi_0 > 0.4$. As for straight trajectories, hydrodynamic interactions push the target, which renders a close approach increasingly difficult with increasing helical slope, but the pusher pair swims stable in a cooperative manner (see Supplementary Movie 4).

The squirmer configuration also affects the helical trajectory of the target. Especially, a target velocity along the distance vector $\mathbf{r}_c$, $v^{\mathrm{ind}} = \langle \mathbf{v}_t \cdot \mathbf{e}_c \rangle$, is induced, which is largest for pushers (Fig. 3d). This additional force on the target affects the properties of its trajectory. Although the helix radius is hardly affected for $\alpha = 1$, the pitch increases substantially for $\xi_0 \lesssim 0.5$, particularly for pushers (Fig. 3e).

The properties of the pursuer-target pair and the target trajectory also depend on the speed ratio $\alpha = v_t/v_p$ (see Supplementary Note 2, Fig. S5**a** for $\xi_0 = 0.4$), with a qualitatively similar dependence as in Fig. 3, with α instead of ξ_0. For any kind of squirmer pair, the pursuer traverses a shorter path than the target, which allows it to follow the target even for $\alpha > 1$. The induced velocity v^{ind} decreases with increasing α due to the weaker steric and hydrodynamic effects, in particular for $\alpha > 1$, where the pursuer propulsion speed is smaller than that of the target (see Fig. S5**a-iii**).

Propulsion direction alignment and speed adaptation. The collective motion of flocks of birds or school of fish is governed by various interactions. In particular, the alignment of the moving direction of an individual with its neighbors plays a fundamental role[72–76]. Theoretically, it has been shown in the Vicsek model[39,77] and its extensions[41,42,54,78] that such an interaction can lead to a preferred direction of motion with broken rotational symmetry. Particle-based alignment models typically neglected hydrodynamic interactions[41,42], which, however, are essential for the emergent collective behavior of microswimmers[8,9]. Here, we address the influence of the microswimmer flow field on the cooperative motion of self-aligning squirmers and propose an adaptation scheme for stable motion.

As the cooperative motion is always unstable for initially aligned squirmers[40,53,61–63,65] as well as for self-steering, persistently aligned squirmers (see Supplementary Note 3, Sec. S-IVB1 for more details), we introduce a speed-adaption mechanism for the iSquirmer to achieve stable pursuit. Applying a velocity relaxation mechanism (see Methods, Eqs. (19), (22)), the propulsion speed $v_p(t)$ of the iSquirmer is changed by accelerating/decelerating it, depending on its position with respect to the target expressed by the scalar product $\mathbf{e}_p \cdot \mathbf{e}_c$. As long as the pursuer is behind the target, $\mathbf{e}_p \cdot \mathbf{e}_c < 0$, it is accelerated, and while if it is in front, $\mathbf{e}_p \cdot \mathbf{e}_c > 0$, it is slowed down. An example for the probability of the pursuer position is presented in Fig. 4a-i and a trajectory in Fig. 5a-i. Note that $\mathbf{e}_p$ and $\mathbf{e}_t$ are nearly parallel for the considered maneuverability. The propulsion velocity is limited by a maximum value v_{max} (see Methods, Eq. (19)).

A stable cooperative state requires an effective attraction between the microswimmers. Thus, no stable state is possible even for aligned propulsion directions of hard-sphere-like ABP particles. Pullers would require a head-to-tail arrangement for stable motion, which, however, already turns out to be unstable for persistently aligned squirmers via self-steering (see Supplementary Note 3, Section S-IVB1). Likewise, the proposed alignment scheme fails to yield a stable cooperative motion for pushers. Such a stable cooperative state is achieved for pushers by the proposed speed adaptation, where their relative arrangement depends on the maximum speed v_{max}. Figure 4a-i, 4a-ii presents the probability distribution function of the pursuer position in cylindrical coordinates, and the pursuer-target flow field, respectively. For speed ratios $v_{max}/v_t > 1$, the pursuer is able to follow the target despite the presence of noise. The distance r_c strongly depends on v_{max} and the probability distribution is broad — the pursuer is even touching the target —, as shown in Fig. 4b. The maximum of the distribution and the average distance decreases with increasing v_{max}, depending only weakly on the Péclet number (Fig. 4c). This is related to a change of the relative arrangement of the squirmers. For smaller v_{max} and larger r_c, the squirmers preferentially assume a head-to-tail configuration, as expressed by the distribution function of the $\mathbf{e}_t \cdot \mathbf{e}_c$ and the corresponding order parameter $\langle \mathbf{e}_t \cdot \mathbf{e}_c \rangle$ in Fig. 4d, e, see also Supplementary Movie 5. However, the distribution function $P(\mathbf{e}_t \cdot \mathbf{e}_c)$ exhibits a long tail toward small values of $\mathbf{e}_t \cdot \mathbf{e}_c$. Already for a small enhanced pursuer speed, $v_{max}/v_t \approx 1.2$, the pursuer is able to surpass the target, which implies a transition between pursuer-target repulsion and attraction (Fig. 4a-i). It is this dynamics, which leads to a stationary cooperative motion. With increasing v_{max}, the distance $\langle r_c \rangle$ and the average $\langle \mathbf{e}_t \cdot \mathbf{e}_c \rangle$ decrease. At the same time, the maximum of the distribution function $P(\mathbf{e}_t \cdot \mathbf{e}_c)$ shifts to smaller arguments, and the pursuer and target preferentially assume a side-by-side configuration, where the two squirmers touch (Fig. 4a-i, b) and attract each other.

Speed adaptation partially cancels far- and near-field hydrodynamic forces between pursuer and target. However, steering and speed adaptation of the pursuer still give rise to a hydrodynamic torque on the target. A pursuer moving behind the target ($\langle \mathbf{e}_p \cdot \mathbf{e}_c \rangle > 0$), rotates the target propulsion direction toward the opposite side of the pursuer (Fig. 5a-ii), i.e., $\mathbf{e}_t$ changes. The reverse effect on the pursuer is small, because steering nearly compensates the torque at large enough maneuverability. Figure 5b displays the temporal autocorrelation function of the propulsion vector $\mathbf{e}_t$, illustrating the strong correlations in its dynamics, with circular parts of the trajectory (Fig. 5a-i, Supplementary Movie 6). The period of oscillatory behavior of the correlation function first decreases with increasing v_{max}, then increases again for larger values, which corresponds to an increase and subsequent decrease of the curvature of the trajectory with v_{max}. This is also reflected in the induced target angular frequency

$$\Omega_t^{ind} = \frac{1}{D_R} \left\langle \mathbf{\Omega}_t \cdot \frac{\mathbf{e}_p \times \mathbf{e}_t}{|\mathbf{e}_p \times \mathbf{e}_t|} \right\rangle, \qquad (6)$$
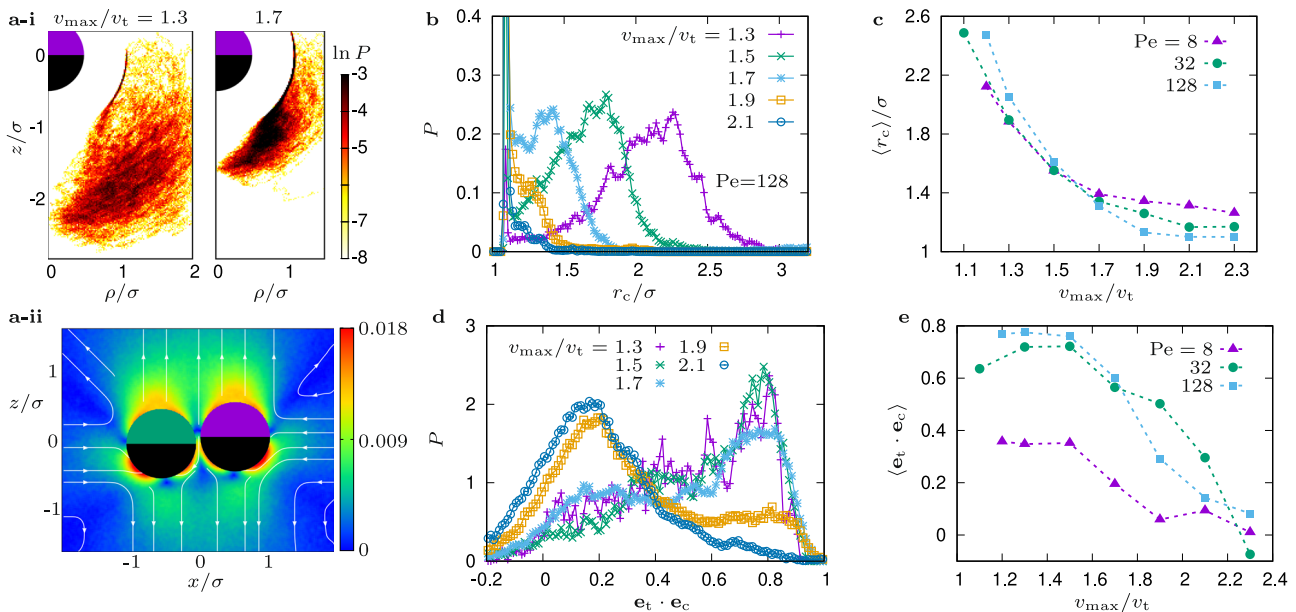

Fig. 4 Pusher cooperative swimming by propulsion-direction alignment and speed adaption. a-i Probability distribution of the pursuer position in cylindrical coordinates. The target is located at the origin of the reference frame. **a-ii** Flow field of the pusher pair for $v_{max}/v_t = 2.3$. **b** Probability distribution of the pursuer-target distance for the indicated speed ratios, where v_{max} is the maximum of the adjustable pursuer speed. **c** Mean pursuer-target distance as a function of the maximum speed v_{max} and Pe = 8 (purple triangles), 32 (green bullets), 128 (blue squares). **d** Probability distribution of $\mathbf{e}_t \cdot \mathbf{e}_c$ for various v_{max}. **e** Order parameter $\langle \mathbf{e}_t \cdot \mathbf{e}_c \rangle$ as function of v_{max} for Pe = 8 (purple triangles), 32 (green bullets), and 128 (blue squares). Here, $\Omega = 75.9$ and $\kappa = 1$ in all cases, and Pe = 128 in (**a, b, d**).
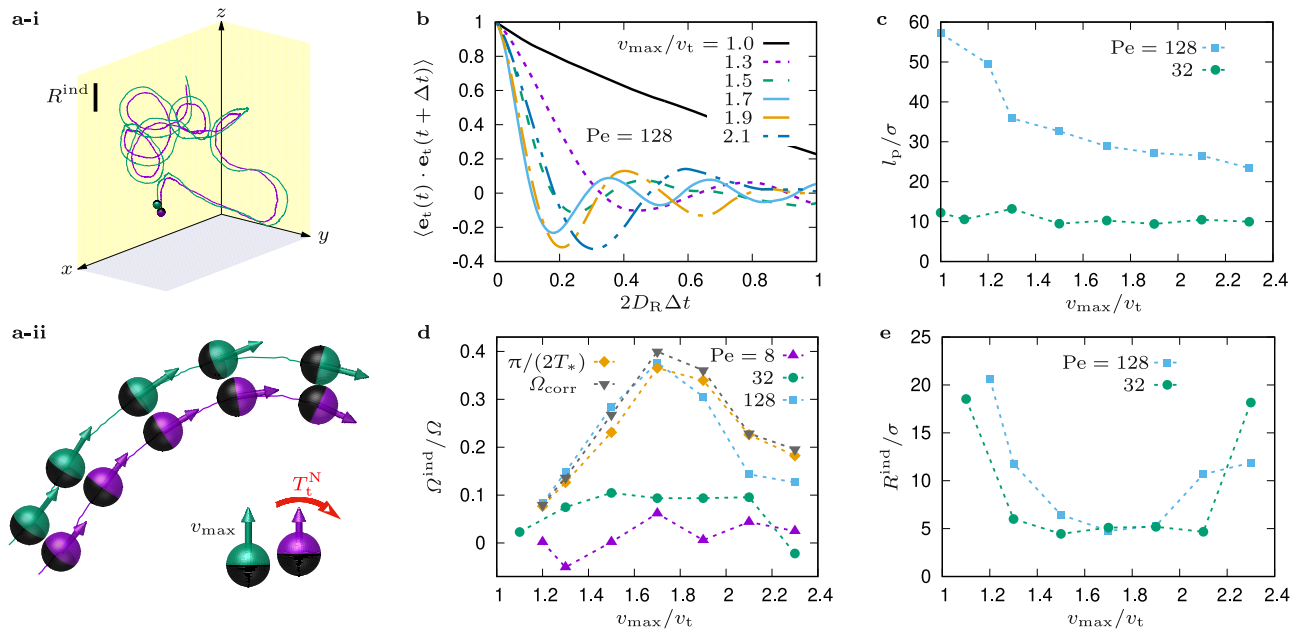
Fig. 5 Pusher cooperative swimming by propulsion-direction alignment and speed adaption. a Emergence of cooperative circular motion. **a-i** Example trajectory, where the vertical black bar represents the radius of induced circular motion (Fig. 5e). **a-ii** Illustration of curvilinear trajectories induced by the torque $\mathbf{T}_t^N$ (red arrow, bottom-right) of the pursuer (petrol) with v_{max} exerted on the target (purple). The pursuer is behind the target. **b** Temporal autocorrelation function of the target propulsion direction $\mathbf{e}_t$ as a function of the lag-time Δt, for Pe = 128 and various v_{max}, where D_R is the rotational diffusion coefficient of an individual squirmer. **c** Persistence length l_p obtained from the characteristic short-time decay of the velocity autocorrelation function. Here, the function $\exp(-\Delta t/\tau)\cos(\Omega_{corr}\Delta t)$ with the persistence time τ and the angular frequency Ω_{corr} is fitted to the data at short times $\langle \mathbf{e}_t(t)\cdot\mathbf{e}_t(t+\Delta t)\rangle < 1/e$ (see Supplementary Note 3, Sec. S-IVC and Fig. S8), from which l_p is obtained as $l_p = v_t\tau$. **d** Induced rotational frequency Ω_t^{ind}, obtained from Eq. (6) as a function of v_{max} for various Péclet numbers as indicated (purple, green, and blue symbols), as well as extracted from the velocity autocorrelation functions in **b**. For the latter, the first zero (T_*) of the velocity autocorrelation function (dark yellow symbols), and Ω_{corr} of the initial decay obtained from the fitting for the persistence length in **c** (gray symbols) are employed to determine the rotational frequency. **e** Radii of induced circular motion determined from $R^{ind} = v_t/\Omega^{ind}$. In all cases, $\Omega = 75.9$ and $\kappa = 1$.

which is essentially a near-field effect (see Supplementary Note 3, Section S-IVB2). Figure 5d confirms the presence of maximum in the angular velocity for large Péclet numbers, and shows that the hydrodynamic effect can be as large as 38% of the pursuer's maneuverability. Thus, the propulsion direction and trajectory of a microswimmer can be manipulated hydrodynamically by a pursuing pusher microswimmer. However, the hydrodynamic effects also render the dynamics more noisy by perturbing the target motion, which may obscure the circular motion, in particular for small Pe and small r_c. Quantitatively, this is captured by the persistence length, which we determine via the characteristic decay time of the velocity autocorrelation function (Fig. 5c), and the diameter of the circular motion due to the induced angular velocity (Fig. 5e). For Pe = 32, the persistence length is essentially independent of v_{max}, whereas for Pe = 128, l_p decreases with increasing v_{max}. This happens because the pursuer-target distance decreases with increasing v_{max} (Fig. 4c), so that larger Pe induce a larger effective noise.

A similar hydrodynamic effect has been found for two or more sedimenting colloidal particles or connected chains of colloids in a viscous fluid. This implies, for example, that sedimenting colloids with a small vertical displacement do not follow the direction of the gravitational field, but sediment with a sideways drift, while sedimenting semiflexible colloid chains can even display helical trajectories[79,80].

Discussion
We have analyzed the interplay of hydrodynamic propulsion, cognition and self-steering, limited maneuverability, hydrodynamic interactions, and thermal or active noise, for a system of

two microswimmers — a moving target and a self-steering pursuer. Both microswimmers are modeled as squirmers, where the pursuer is able to adjust its hydrodynamic propulsion to follow the target. Implicitly sensed information about either the target position or the orientation of its propulsion direction is employed for steering of the pursuer through a non-axisymmetric modification of the surface slip velocity. The squirmer's hydrodynamic propulsion type (pusher or puller) together with the steering mechanism determines the emerging cooperative states.

More specifically, for pursuers with active reorientation of its propulsion direction toward the target, we show that pullers are able to catch up with the target, which is advantageous for a predator to reach its prey. In contrast, for pushers the average pursuer-target distance is typically found to be finite, with the formation of stable cooperatively moving pairs — and the only option for the pursuer to catch up with the target is for speeds much larger than the target speed. This is related to the problem of starving fish larvae, which are typically pushers.

For steering through alignment of the propulsion direction, the pursuit of a moving target is predicted to be always unstable for pullers, while it can lead to stable cooperative motion for pushers — but only in combination with speed adaptation. Here, indirect steering of the target is possible via hydrodynamic torques exerted by the pursuer. This effect could be utilized for microbots for the guidance of active target particles toward a preselected location.

Hydrodynamic interactions between the squirmers and thermal noise strongly influence their cooperative behavior, and is crucial for the emergent dynamics in systems of self-propelled microorganisms with information exchange. Our analysis of the various steering and adaptation schemes provides insight into useful pursuit strategies, and, in particular, reveals ineffective

strategies. This may help in the design of synthetic, information processing microrobots at low Reynolds numbers, where hydrodynamic interactions and thermal fluctuations are paramount.

In our study, we have employed a very simple cognitive rule. The cognitive capacity of these model microswimmers can be increased by extending our model in various ways, for example by incorporating a larger number of input signals, like the (vectorial) target velocity, which will allow the extrapolation of current target location and motion to future positions, as well as by employing more sophisticated adaptation rules other than simply turning toward the target direction. More complex and convoluted cognitive relations between input signals and output actions must then be developed accordingly. In particular, it will be interesting to see whether it will be possible to devise cognitive functions which anticipate hydrodynamic interactions, and thereby help a predator to catch a prey in a fluid. Machine-learning approaches should be very helpful in this respect.

Methods

Intelligent squirmer (iSquirmer). The dynamics of a squirmer is governed by its surface flow field $\mathbf{u}_{sq}$[32–34]. In case of a spherical, non-axisymmetric squirmer of radius R_{sq}, which translates and rotates, the spherical components of the surface slip velocity in a body-fixed reference frame are $(\mathbf{u}_{sq} = (u_\theta, u_\phi, 0)^T)$[34]

$$u_\theta = B_1 \sin\theta(1 + \beta\cos\theta) - \frac{1}{R_{sq}^2}(\tilde{C}_{11}\cos\phi - C_{11}\sin\phi), \quad (7)$$

$$u_\phi = \frac{\cos\theta}{R_{sq}^2}(C_{11}\cos\phi + \tilde{C}_{11}\sin\phi) + \frac{\sin\theta}{R_{sq}^2}C_{01}, \quad (8)$$

where θ and ϕ are the polar and azimuthal angles. $B_1 = 3v_0/2$ determines the magnitude of the self-propulsion velocity v_0 and β the stresslet, where $\beta > 0$ for pullers and $\beta < 0$ pushers. The non-axisymmetric components C and $\tilde{C}$ are associated with the angular velocity

$$\boldsymbol{\omega}_0 = \frac{1}{R_{sq}^3}(C_{11}\mathbf{e}_x + \tilde{C}_{11}\mathbf{e}_y - C_{01}\mathbf{e}_z), \quad (9)$$

of the squirmer body. In a Cartesian laboratory reference frame, with an instantaneous squirmer motion along the z direction, the parameters C_{01}, C_{11}, and $\tilde{C}_{11}$ determine the angular velocity along the unit vectors $\mathbf{e}_x$, $\mathbf{e}_y$, and $\mathbf{e}_z$ of the axis of the reference frame.

Steering of a squirmer, in the spirit of the cognitive flocking model[35,36], is achieved by a modification of the surface flow field. Biological microswimmers, such as *Chlamydomonas* and *Volvox* algae, stir the ambient fluid in the opposite side of the direction they intend to turn to. For an intelligent squirmer (iSquirmer) with limited maneuverability, the required angular velocity is given by Eq. (1). The corresponding adaptation of propulsion is achieved by equating the non-axisymmetric components of surface flow field of Eq. (9) with Eq. (1), which yields

$$C_{11} = C_0 R_{sq}^3 (\mathbf{e}_p \times \mathbf{e}_{aim}) \cdot \mathbf{e}_x, \quad (10)$$

$$\tilde{C}_{11} = C_0 R_{sq}^3 (\mathbf{e}_p \times \mathbf{e}_{aim}) \cdot \mathbf{e}_y, \quad (11)$$

$$C_{01} = 0. \quad (12)$$

Note that the rotation around the squirmer body axis, determined by C_{01}, is irrelevant, because it does not affect the self-propulsion direction.

In case of pursuit as in the cognitive flocking model, the propulsion direction is oriented toward the target position (see

Fig. 1d-i), hence,

$$\mathbf{e}_{aim} = \mathbf{e}_c = \frac{\mathbf{r}_c}{|\mathbf{r}_c|}, \quad (13)$$

where $\mathbf{r}_c = \mathbf{r}_t - \mathbf{r}_p$ denotes the vector connecting the pursuer and target positions $\mathbf{r}_p$ and $\mathbf{r}_t$ (Fig. 1a).

Velocity alignment, as in the Vicsek model[39], is achieved by the condition

$$\mathbf{e}_{aim} = \mathbf{e}_t, \quad (14)$$

see Fig. 1d-ii. Here, in the absence of both noise and hydrodynamic interactions, the two active agents become perfectly aligned and self-propel along the common direction at the same velocity.

Squirmer on helical trajectory. A target moving on a helical trajectory of radius R, pitch H, and slope $\xi = H/(2\pi R)$ is achieved by the choice of its surface flow field:

$$C_{01} = \frac{R_{sq}^2}{2}\frac{\xi}{1 + \xi^2}v_t, \quad C_{11} = \frac{R_{sq}^2}{2}\frac{1}{1 + \xi^2}v_t, \quad (15)$$

$$\tilde{C}_{11} = 0. \quad (16)$$

The corresponding helix parameters are

$$R = \frac{\sqrt{(C_{11})^2 + (\tilde{C}_{11})^2}}{(C_{11})^2 + (\tilde{C}_{11})^2 + (C_{01})^2}v_t R_{sq}^3, \quad (17)$$

$$H = \frac{2\pi C_{01}}{(C_{11})^2 + (\tilde{C}_{11})^2 + (C_{01})^2}v_t R_{sq}^3. \quad (18)$$

Pursuer speed adaptation. We model the speed adaptation ability of the iSquirmer by a continuous-time acceleration/deceleration process:

$$\dot{v}_p(t) = \begin{cases} \kappa\frac{v_{max} - v_p(t)}{R_{sq}}v_p(t), & \text{for } \mathbf{e}_p \cdot \mathbf{e}_c \geq 0, \\ -\kappa\frac{v_p(t)}{R_{sq}}v_p(t), & \text{for } \mathbf{e}_p \cdot \mathbf{e}_c < 0. \end{cases} \quad (19)$$

The (dimensionless) friction coefficient κ and the maximum speed v_{max} account for a limited speed-adaptation capacity. With an initial condition $v_p(0) = v_p^0$, the above equations imply

$$v_p(t) = v_{max}\left[1 + (v_{max}/v_p^0 - 1)\exp(-v_{max}(\kappa/R_{sq})t)\right]^{-1} \quad (20)$$

for persistent acceleration, and

$$v_p(t) = \left[1/v_p^0 + (\kappa/R_{sq})t\right]^{-1} \quad (21)$$

for persistent deceleration, respectively. Numerically, the speed $v_p(t)$ is obtained by the Euler scheme

$$v_p(t + h) = v_p(t) + h\dot{v}_p(t), \quad (22)$$

with the MPC collision time h. As initial condition, we choose $v_p(0) = v_t$.

Steric squirmer repulsion. Steric squirmer-squirmer interactions are described by the separation-shifted Lennard-Jones potential

$$U_{LJ}(d_s) = 4\epsilon_0\left[\left(\frac{\sigma_0}{d_s + \sigma_0}\right)^{12} - \left(\frac{\sigma_0}{d_s + \sigma_0}\right)^6 + \frac{1}{4}\right], \quad (23)$$

for $d_s < (2^{1/6} - 1)\sigma_0$ and zero otherwise. The distance d_s between the two closest points on the surfaces of two interacting spheres is chosen as $d_s = r_c - \sigma - 2d_v$, where σ is the diameter of a squirmer, r_c the center-to-center distance between the two squirmers, and

d_v a virtual safety distance to prevent loss of hydrodynamic interactions at close distances[8,63,81].

The solid-body equations of motion of the squirmers, their center-of-mass translational and their rotational motion described by quaternions, are solved by the velocity-Verlet algorithm[63,81].

Fluid model: multiparticle collision dynamics. The fluid is modeled via the multiparticle collision dynamics (MPC) method, a particle-based mesoscale simulation approach accounting for thermal fluctuations[55,56], which has been applied in various simulation studies of active matter[9,60,69,82–87]. The MPC fluid properties agree with those obtained from the Navier-Stokes equations on length scales larger than the collision-cell size[57]. Similarly, simulations of colloids in the bulk[88] and at interfaces[89] yield agreement with predictions of the Navier-Stokes equations, in particular, lubrication is correctly accounted for.

We apply the stochastic rotation variant of the MPC approach with angular momentum conservation (MPC-SRD+a)[9,59,90]. The algorithm proceeds in two steps — streaming and collision. In the streaming step, the MPC point particles of mass m propagate ballistically over a time interval h, denoted as collision time. In the collision step, fluid particles are sorted into the cells of a cubic lattice of lattice constant a defining the collision environment, and their relative velocities, with respect to the center-of-mass velocity of the collision cell, are rotated around a randomly oriented axes by a fixed angle α. The algorithm conserves mass, linear, and angular momentum on the collision-cell level, which implies hydrodynamics on large length and long time scales[55,57]. A random shift of the collision cell lattice is applied at every collision step to ensure Galilean invariance[91]. Thermal fluctuations are intrinsic to the MPC method. A cell-level canonical thermostat (Maxwell-Boltzmann scaling (MBS) thermostat) is applied after every collision step, which maintains the temperature at the desired value[92]. The MPC method is highly parallel and is efficiently implemented on a graphics processing unit (GPU) for a high-performance gain[93].

Squirmer-fluid interactions appear during streaming and collision. While streaming squirmers and fluid particles, fluid particles are reflected at a squirmer's surface by applying the bounce-back rule and adding the surface velocity $\mathbf{u}_{sq}$. To minimize slip, phantom particles are added inside of the squirmers, which contribute when collision cells penetrate squirmers. In all cases, the total linear and angular momenta are included in the squirmer dynamics. More details are described by Theers et al.[63] and the supplementary material of Qi et al.[81].

Simulation setup and parameters. The average number of MPC particles in a collision cell is chosen as $\langle N_c \rangle = 50$, the collision time as $h = 0.02a\sqrt{m/(k_BT)}$, and the rotation angle as $\alpha_c = 130°$, where a is the length of a cubic collision cell, T the temperature, and k_B the Boltzmann constant[8]. These values yield the fluid viscosity of $\eta = 111.3\sqrt{mk_BT/a^2}$[90,94] (cf. Supplementary Methods for more details of the MPC algorithm). With the squirmer radius $R_{sq} = 3a$, the theoretical rotational diffusion coefficient is given as $D_R = 1.3 \times 10^{-5}\sqrt{k_BT/m}/a$, in close agreement with simulation results[8]. We consider the Péclet numbers Pe = 8, 32, and 128, and the magnitude of the active stress $|\beta| = 3$. In all simulations, the Reynolds number is smaller than Re = 0.03. The considered values of Pe and β are comparable with estimates from experiments on diffusiophoretic Janus particles[95,96] and bacteria[97], as discussed in Refs. [9,98]. The ratio Pe/Ω determines the curvature of the pursuer trajectory[36]. In experiments on microrobots, radii of the pursuer trajectory are roughly

comparable to the size of a microrobot[28], indicating that the maneuverability can be as large as $\Omega \approx$ Pe. Accordingly, we present results for $\Omega \le 4$ Pe in the main text, and discuss results up to $\Omega = 32$ Pe in the Supplementary Information. The length of the three-dimensional cubic simulation box is $L_b = 48a = 16R_{sq}$, and periodic boundary conditions are applied.

The parameters of the Lennard-Jones potential (23) are set to $\sigma_0 = 0.5a$, $\epsilon_0 = 5k_BT$, and $d_v = 0.25a$.

A passive sphere is neutrally buoyant with mass $M = 5655m$, where m is the mass of a MPC particle, and the MPC time step h is used in the integration of the squirmers' equations of motion.

For the aiming strategy where longitudinal hydrodynamic effects are critical, we consider the initial condition where a pursuer aligned parallel to the target, i.e., $\mathbf{e}_p = \mathbf{e}_t$, is located behind the target with the distance $r_{init} = 2\sigma$. On the other hand, for the alignment strategy where hydrodynamic effects in transverse directions are dominant, target-pursuer pairs are initially arranged in a side-by-side configuration with the distance $r_{init} = 2\sigma$ and $\mathbf{e}_p = \mathbf{e}_t$. We ran simulations up to $t D_R = 1.2$ for Pe = 32 and 128, and $t D_R = 5.0$ for Pe = 8. Obtained results are averaged over at least 10 realizations. The initial 20% of each trajectory are discarded in the analysis.

Data availability

The data that support the findings of this study are available from the corresponding author upon reasonable request.

Code availability

The code employed in this study is available from the corresponding author upon reasonable request.

References

1. Tuval, I. et al. Bacterial swimming and oxygen transport near contact lines. *Proc. Natl. Acad. Sci. USA* **102**, 2277 (2005).
2. Guasto, J. S., Johnson, K. A. & Gollub, J. P. Oscillatory flows induced by microorganisms swimming in two dimensions. *Phys. Rev. Lett.* **105**, 168102 (2010).
3. Kiørboe, T., Jiang, H., Gonçalves, R. J., Nielsen, L. T. & Wadhwa, N. Flow disturbances generated by feeding and swimming zooplankton. *Proc. Natl. Acad. Sci. USA* **111**, 11738 (2014).
4. Elgeti, J., Winkler, R. G. & Gompper, G. Physics of microswimmers—single particle motion and collective behavior: a review. *Rep. Prog. Phys.* **78**, 056601 (2015).
5. Bechinger, C. et al. Active particles in complex and crowded environments. *Rev. Mod. Phys.* **88**, 045006 (2016).
6. China, V. & Holzman, R. Hydrodynamic starvation in first-feeding larval fishes. *Proc. Natl. Acad. Sci. USA* **111**, 8083 (2014).
7. Kiørboe, T., Andersen, A., Langlois, V. J., Jakobsen, H. H. & Bohr, T. Mechanisms and feasibility of prey capture in ambush-feeding zooplankton. *Proc. Natl. Acad. Sci. USA* **106**, 12394 (2009).
8. Theers, M., Westphal, E., Qi, K., Winkler, R. G. & Gompper, G. Clustering of microswimmers: interplay of shape and hydrodynamics. *Soft Matter* **14**, 8590 (2018).
9. Qi, K., Westphal, E., Gompper, G. & Winkler, R. G. Emergence of active turbulence in microswimmer suspensions due to active hydrodynamic stress and volume exclusion. *Commun. Phys.* **5**, 49 (2022).
10. Samatas, S. & Lintuvuori, J. Hydrodynamic synchronization of chiral microswimmers. *Phys. Rev. Lett.* **130**, 024001 (2023).
11. Wensink, H. H. et al. Meso-scale turbulence in living fluids. *Proc. Natl. Acad. Sci. USA* **109**, 14308 (2012).
12. Dunkel, J. et al. Fluid dynamics of bacterial turbulence. *Phys. Rev. Lett.* **110**, 228102 (2013).
13. Aranson, I. S. Bacterial active matter. *Rep. Prog. Phys.* **85**, 076601 (2022).

14. Ricotti, L. et al. Biohybrid actuators for robotics: A review of devices actuated by living cells. *Sci. Robot.* **2**, eaaq0495 (2017).
15. Huang, T.-Y., Gu, H. & Nelson, B. J. Increasingly intelligent micromachines. *Annu. Rev. Control Robot. Auton. Syst.* **5**, 279 (2022).
16. Bäuerle, T., Fischer, A., Speck, T. & Bechinger, C. Self-organization of active particles by quorum sensing rules. *Nat. Commun.* **9**, 3232 (2018).
17. Selmke, M., Khadka, U., Bregulla, A. P., Cichos, F. & Yang, H. Theory for controlling individual self-propelled micro-swimmers by photon nudging I: directed transport. *Phys. Chem. Chem. Phys.* **20**, 10502 (2018).
18. Lavergne, F. A., Wendehenne, H., Bäuerle, T. & Bechinger, C. Group formation and cohesion of active particles with visual perception–dependent motility. *Science* **364**, 70 (2019).
19. Kaspar, C., Ravoo, B. J., van der Wiel, W. G., Wegner, S. V. & Pernice, W. H. P. The rise of intelligent matter. *Nature* **594**, 345 (2021).
20. Erkoc, P. et al. Mobile microrobots for active therapeutic delivery. *Adv. Ther.* **2**, 1800064 (2019).
21. Kurzthaler, C. et al. A geometric criterion for the optimal spreading of active polymers in porous media. *Nat. Commun.* **12**, 7088 (2021).
22. Cvetkovic, C. et al. Three-dimensionally printed biological machines powered by skeletal muscle. *Proc. Natl. Acad. Sci. USA* **111**, 10125 (2014).
23. Hinz, R. C. & de Polavieja, G. G. Ontogeny of collective behavior reveals a simple attraction rule. *Proc. Natl. Acad. Sci. USA* **114**, 2295–2300 (2017).
24. Kiørboe, T. How zooplankton feed: mechanisms, traits and trade-offs. *Biol. Rev.* **86**, 311–339 (2011).
25. van Leeuwen, J. L., Voesenek, C. J. & Müller, U. K. How body torque and Strouhal number change with swimming speed and developmental stage in larval zebrafish. *J. R. Soc. Interface* **12**, 20150479 (2015).
26. Jikeli, J. F. et al. Sperm navigation along helical paths in 3D chemoattractant landscapes. *Nat. Commun.* **6**, 7985 (2015).
27. Garcia-Seyda, N. et al. Human neutrophils swim and phagocytise bacteria. *Biol. Cell* **113**, 28–38 (2021).
28. Pellicciotta, N. et al. Light controlled biohybrid microbots. *Adv. Funct. Mater.* **2023**, 2214801 (2023).
29. Dai, B. et al. Programmable artificial phototactic microswimmer. *Nat. Nanotechnol.* **11**, 1087 (2016).
30. Tsang, A. C. H., Lam, A. T. & Riedel-Kruse, I. H. Polygonal motion and adaptable phototaxis via flagellar beat switching in the microswimmer *Euglena gracilis*. *Nat. Phys.* **14**, 1216 (2018).
31. Alvarez, L. et al. Reconfigurable artificial microswimmers with internal feedback. *Nat. Commun.* **12**, 4762 (2021).
32. Lighthill, M. J. On the squirming motion of nearly spherical deformable bodies through liquids at very small Reynolds numbers. *Comm. Pure Appl. Math.* **5**, 109 (1952).
33. Blake, J. R. A spherical envelope approach to ciliary propulsion. *J. Fluid Mech.* **46**, 199 (1971).
34. Pak, O. S. & Lauga, E. Generalized squirming motion of a sphere. *J. Eng. Math.* **88**, 1 (2014).
35. Barberis, L. & Peruani, F. Large-scale patterns in a minimal cognitive flocking model: Incidental leaders, nematic patterns, and aggregates. *Phys. Rev. Lett.* **117**, 248001 (2016).
36. Goh, S., Winkler, R. G. & Gompper, G. Noisy pursuit and pattern formation of self-steering active particles. *N. J. Phys.* **24**, 093039 (2022).
37. Singh Negi, R., Winkler, R. G. & Gompper, G. Emergent collective behavior of active Brownian particles with visual perception. *Soft Matter* **18**, 6167 (2022).
38. Gassner, A., Goh, S., Gompper, G. & Winkler, R. G. Noisy pursuit by a self-steering active particle in confinement. *EPL* **142**, 21002 (2023).
39. Vicsek, T., Czirók, A., Ben-Jacob, E., Cohen, I. & Shochet, O. Novel type of phase transition in a system of self-driven particles. *Phys. Rev. Lett.* **75**, 1226 (1995).
40. Aditi Simha, R. & Ramaswamy, S. Hydrodynamic fluctuations and instabilities in ordered suspensions of self-propelled particles. *Phys. Rev. Lett.* **89**, 058101 (2002).
41. Chaté, H. Dry aligning dilute active matter. *Annu. Rev. Condens. Matter Phys.* **11**, 189 (2020).
42. Chepizhko, O., Saintillan, D. & Peruani, F. Revisiting the emergence of order in active matter. *Soft Matter* **17**, 3113 (2021).
43. Garnier, S., Combe, M., Jost, C. & Theraulaz, G. Do ants need to estimate the geometrical properties of trail bifurcations to find an efficient route? A swarm robotics test bed. *PLoS Comput. Biol.* **9**, 1–12 (2013).
44. Lyon, P. The cognitive cell: bacterial behavior reconsidered. *Front. Microbiol.* **6**, 264 (2015).
45. Bechtel, W. & Bich, L. Grounding cognition: heterarchical control mechanisms in biology. *Philos. Trans. R. Soc. B* **376**, 20190751 (2021).
46. Li, Z. et al. Self-sensing intelligent microrobots for noninvasive and wireless monitoring systems. *Microsyst. Nanoeng.* **9**, 102 (2023).
47. Zhu, G., Fang, W.-Z. & Zhu, L. Optimizing low-Reynolds-number predation via optimal control and reinforcement learning. *J. Fluid Mech.* **944**, A3 (2022).
48. Borra, F., Biferale, L., Cencini, M. & Celani, A. Reinforcement learning for pursuit and evasion of microswimmers at low Reynolds number. *Phys. Rev. Fluids* **7**, 023103 (2022).
49. Menzel, R. et al. Honey bees navigate according to a map-like spatial memory. *Proc. Natl. Acad. Sci. USA* **102**, 3040–3045 (2005).
50. Vergassola, M., Villermaux, E. & Shraiman, B. I. 'Infotaxis' as a strategy for searching without gradients. *Nature* **445**, 406 (2007).
51. Torney, C., Neufeld, Z. & Couzin, I. D. Context-dependent interaction leads to emergent search behavior in social aggregates. *Proc. Natl. Acad. Sci. USA* **106**, 22055–22060 (2009).
52. Charlesworth, H. J. & Turner, M. S. Intrinsically motivated collective motion. *Proc. Natl. Acad. Sci. USA* **116**, 15362–15367 (2019).
53. Ishikawa, T., Simmonds, M. P. & Pedley, T. J. Hydrodynamic interaction of two swimming model micro-organisms. *J. Fluid Mech.* **568**, 119 (2006).
54. Shaebani, M. R., Wysocki, A., Winkler, R. G., Gompper, G. & Rieger, H. Computational models for active matter. *Nat. Rev. Phys.* **2**, 181 (2020).
55. Kapral, R. Multiparticle collision dynamics: Simulations of complex systems on mesoscale. *Adv. Chem. Phys.* **140**, 89 (2008).
56. Gompper, G., Ihle, T., Kroll, D. M. & Winkler, R. G. Multi-particle collision dynamics: A particle-based mesoscale simulation approach to the hydrodynamics of complex fluids. *Adv. Polym. Sci.* **221**, 1 (2009).
57. Huang, C.-C., Gompper, G. & Winkler, R. G. Hydrodynamic correlations in multiparticle collision dynamics fluids. *Phys. Rev. E* **86**, 056711 (2012).
58. Noguchi, H., Kikuchi, N. & Gompper, G. Particle-based mesoscale hydrodynamic techniques. *EPL* **78**, 10005 (2007).
59. Theers, M., Westphal, E., Gompper, G. & Winkler, R. G. From local to hydrodynamic friction in Brownian motion: A multiparticle collision dynamics simulation study. *Phys. Rev. E* **93**, 032604 (2016).
60. Hu, J., Yang, M., Gompper, G. & Winkler, R. G. Modelling the mechanics and hydrodynamics of swimming *E. coli*. *Soft Matter* **11**, 7867 (2015).
61. Llopis, I. & Pagonabarraga, I. Hydrodynamic interactions in squirmer motion: Swimming with a neighbour and close to a wall. *J. Non-Newton. Fluid Mech.* **165**, 946 (2010).
62. Götze, I. O. & Gompper, G. Mesoscale simulations of hydrodynamic squirmer interactions. *Phys. Rev. E* **82**, 041921 (2010).
63. Theers, M., Westphal, E., Gompper, G. & Winkler, R. G. Modeling a spheroidal microswimmer and cooperative swimming in a narrow slit. *Soft Matter* **12**, 7372 (2016).
64. Clopés, J., Gompper, G. & Winkler, R. G. Hydrodynamic interactions in squirmer dumbbells: active stress-induced alignment and locomotion. *Soft Matter* **16**, 10676 (2020).
65. Saintillan, D. & Shelley, M. J. Instabilities and pattern formation in active particle suspensions: Kinetic theory and continuum simulations. *Phys. Rev. Lett.* **100**, 178103 (2008).
66. Turner, L., Ryu, W. S. & Berg, H. C. Real-time imaging of fluorescent flagellar filaments. *J. Bacteriol.* **182**, 2793 (2000).
67. Bianchi, S., Saglimbeni, F. & Di Leonardo, R. Holographic imaging reveals the mechanism of wall entrapment in swimming bacteria. *Phys. Rev. X* **7**, 011010 (2017).
68. Mathijssen, A. J. T. M. et al. Oscillatory surface rheotaxis of swimming E. coli bacteria. *Nat. Commun.* **20**, 3434 (2019).
69. Mousavi, S. M., Gompper, G. & Winkler, R. G. Wall entrapment of peritrichous bacteria: a mesoscale hydrodynamics simulation study. *Soft Matter* **16**, 4866 (2020).
70. Clopés, J. & Winkler, R. G. Flagellar arrangements in elongated peritrichous bacteria: bundle formation and swimming properties. *Eur. Phys. J. E* **44**, 17 (2021).
71. Cortese, D. & Wan, K. Y. Control of helical navigation by three-dimensional flagellar beating. *Phys. Rev. Lett.* **126**, 088003 (2021).
72. Ballerini, M. et al. Empirical investigation of starling flocks: a benchmark study in collective animal behaviour. *Anim. Behav.* **76**, 201–215 (2008).
73. Cavagna, A. & Giardina, I. Bird flocks as condensed matter. *Annu. Rev. Condens. Matter Phys.* **5**, 183 (2014).
74. Papadopoulou, M., Hildenbrandt, H., Sankey, D. W. E., Portugal, S. J. & Hemelrijk, C. K. Self-organization of collective escape in pigeon flocks. *PLoS Comput. Biol.* **18**, e1009772 (2022).
75. Gompper, G. et al. The 2020 motile active matter roadmap. *J. Phys: Condens. Matter* **32**, 193001 (2020).
76. Katz, Y., Tunstrøm, K., Ioannou, C. C., Huepe, C. & Couzin, I. D. Inferring the structure and dynamics of interactions in schooling fish. *Proc. Natl Acad. Sci. USA* **108**, 18720 (2011).
77. Vicsek, T. & Zafeiris, A. Collective motion. *Phys. Rep.* **517**, 71 (2012).
78. Toner, J. & Tu, Y. Long-range order in a two-dimensional dynamical XY model: How birds fly together. *Phys. Rev. Lett.* **75**, 4326 (1995).
79. Ekiel-Jeżewska, M. L., Gubiec, T. & Szymczak, P. Stokesian dynamics of close particles. *Phys. Fluids* **20**, 063102 (2008).
80. Saggiorato, G., Elgeti, J., Winkler, R. G. & Gompper, G. Conformations, hydrodynamic interactions, and instabilities of sedimenting semiflexible filaments. *Soft Matter* **11**, 7337 (2015).

81. Qi, K., Westphal, E., Gompper, G. & Winkler, R. G. Enhanced rotational motion of spherical squirmer in polymer solutions. *Phys. Rev. Lett.* **124**, 068001 (2020).

82. Reigh, S. Y., Winkler, R. G. & Gompper, G. Synchronization and bundling of anchored bacterial flagella. *Soft Matter* **8**, 4363 (2012).

83. Babu, S. B. & Stark, H. Modeling the locomotion of the African trypanosome using multi-particle collision dynamics. *N. J. Phys.* **14**, 085012 (2012).

84. Colberg, P. H., Reigh, S. Y., Robertson, B. & Kapral, R. Chemistry in motion: Tiny synthetic motors. *Acc. Chem. Res.* **47**, 3504–3511 (2014).

85. Hu, J., Wysocki, A., Winkler, R. G. & Gompper, G. Physical sensing of surface properties by microswimmers – directing bacterial motion via wall slip. *Sci. Rep.* **5**, 9586 (2015).

86. Eisenstecken, T., Gompper, G. & Winkler, R. G. Conformational properties of active semiflexible polymers. *Polymers* **8**, 304 (2016).

87. Rode, S., Elgeti, J. & Gompper, G. Sperm motility in modulated microchannels. *N. J. Phys.* **21**, 013016 (2019).

88. Poblete, S., Wysocki, A., Gompper, G. & Winkler, R. G. Hydrodynamics of discrete-particle models of spherical colloids: A multiparticle collision dynamics simulation study. *Phys. Rev. E* **90**, 033314 (2014).

89. Padding, J. T. & Briels, W. J. Translational and rotational friction on a colloidal rod near a wall. *J. Chem. Phys.* **132**, 054511 (2010).

90. Noguchi, H. & Gompper, G. Transport coefficients of off-lattice mesoscale-hydrodynamics simulation techniques. *Phys. Rev. E* **78**, 016706 (2008).

91. Ihle, T. & Kroll, D. M. Stochastic rotation dynamics I: Formalism, Galilean invariance, Green-Kubo relations. *Phys. Rev. E* **67**, 066705 (2003).

92. Huang, C.-C., Chatterji, A., Sutmann, G., Gompper, G. & Winkler, R. G. Cell-level canonical sampling by velocity scaling for multiparticle collision dynamics simulations. *J. Comput. Phys.* **229**, 168 (2010).

93. Westphal, E., Singh, S. P., Huang, C.-C., Gompper, G. & Winkler, R. G. Multiparticle collision dynamics: GPU accelerated particle-based mesoscale hydrodynamic simulations. *Comput. Phys. Comm.* **185**, 495 (2014).

94. Theers, M. & Winkler, R. G. Bulk viscosity of multiparticle collision dynamics fluids. *Phys. Rev. E* **91**, 033309 (2015).

95. Howse, J. R. et al. Self-motile colloidal particles: From directed propulsion to random walk. *Phys. Rev. Lett.* **99**, 048102 (2007).

96. Ebbens, S., Tu, M.-H., Howse, J. R. & Golestanian, R. Size dependence of the propulsion velocity for catalytic Janus-sphere swimmers. *Phys. Rev. E* **85**, 020401 (2012).

97. Drescher, K., Dunkel, J., Cisneros, L. H., Ganguly, S. & Goldstein, R. E. Fluid dynamics and noise in bacterial cell-cell and cell-surface scattering. *Proc. Natl Acad. Sci. USA* **108**, 10940 (2011).

98. Elgeti, J. & Gompper, G. Wall accumulation of self-propelled spheres. *EPL* **101**, 48003 (2013).

Author contributions

R.G.W. and G.G. designed the research. S.G. performed simulations and analysed the data. All authors discussed results and wrote the manuscript together.

Funding

Competing interests

The authors declare no competing interests.

Additional information

Supplementary information The online version contains supplementary material available at https://doi.org/10.1038/s42005-023-01432-5.

Correspondence and requests for materials should be addressed to Gerhard Gompper.

Peer review information : *Communications Physics* thanks the anonymous reviewers for their contribution to the peer review of this work.

Reprints and permission information is available at http://www.nature.com/reprints

Publisher's note Springer Nature remains neutral with regard to jurisdictional claims in published maps and institutional affiliations.